Astronomy & Astrophysics manuscript no. Census_LBA_v_0.4
September 2, 2019

A LOFAR census of non-recycled pulsars: extending below 80 MHz

A. V. Bilous[1], L. Bondonneau[2], V. I. Kondratiev[3,4], J.-M. Grießmeier[2,5], G. Theureau[2,5,6], M. Kramer[7,8], J. van Leeuwen[1,3], C. Sobey[9,10], B. W. Stappers[8], S. ter Veen[3], and P. Weltevrede[8]

[1] Anton Pannekoek Institute for Astronomy, University of Amsterdam, Science Park 904, 1098 XH Amsterdam, The Netherlands e-mail: A.Bilous@uva.nl
[2] LPC2E - Université d'Orléans / CNRS, 45071 Orléans cedex 2, France
[3] ASTRON, the Netherlands Institute for Radio Astronomy, Postbus 2, 7990 AA Dwingeloo, The Netherlands
[4] Astro Space Centre, Lebedev Physical Institute, Russian Academy of Sciences, Profsoyuznaya Str. 84/32, Moscow 117997, Russia
[5] Station de Radioastronomie de Nançay, Observatoire de Paris, PSL Research University, CNRS, Univ. Orléans, OSUC, 18330 Nançay, France
[6] Laboratoire Univers et Théories LUTh, Observatoire de Paris, CNRS/INSU, Université Paris Diderot, 5 place Jules Janssen, 92190 Meudon, France
[7] Max-Planck-Institut für Radioastronomie, Auf dem Hügel 69, 53121 Bonn, Germany
[8] Jodrell Bank Centre for Astrophysics, School of Physics and Astronomy, University of Manchester, Manchester M13 9PL, UK
[9] International Centre for Radio Astronomy Research - Curtin University, GPO Box U1987, Perth, WA 6845, Australia
[10] CSIRO Astronomy and Space Science, PO Box 1130 Bentley, WA 6102, Australia

September 2, 2019

ABSTRACT

We present the results from the low-frequency (40–78 MHz) extension of the first LOFAR pulsar census of non-recycled pulsars. We have used the Low-Band Antennas of the LOFAR core stations to observe 87 pulsars out of 158 that have been detected previously with the High-Band Antennas. Forty-three pulsars have been detected and we present here their flux densities and calibrated profiles. Seventeen of these pulsars have not been, to our knowledge, observed before at such low frequencies. We re-calculate the spectral indices obtained within the LOFAR census using the new information about low-frequency flux densities and discuss the prospects of studying pulsars at the very low frequencies with the current and upcoming facilities, such as NenuFAR.

Key words. pulsars

1. Introduction

Half a century ago, the work on interplanetary scintillation at the frequency of 81.5 MHz led to the serendipitous discovery of pulsars (Hewish et al. 1968). However, until recently most pulsar observations were conducted at higher frequencies of 300–3000MHz because of instrumental challenges. Properties of pulsar emission at radio frequencies below 200 MHz remained relatively poorly explored for two reasons: the high level of the background Galactic emission, and the deleterious influence of the electron plasma in the interstellar medium (ISM) and Earth's ionosphere.

The last decade brought rapid advances both in hardware and computing capabilities, for the first time allowing broadband sensitive observations of pulsars with compensation for dispersive delay at frequencies below 200 MHz. These observations deepen our understanding of pulsars as astrophysical objects: e.g. changes in spectral shape of radio emission and the morphology of the average pulse shape provide information about the microphysics of pulsar radio emission and magnetospheric configurations. Also, because of their increased effects on the received signal, the ISM and the ionosphere can be more accurately studied at lower frequencies.

The new generation of low-frequency radio telescopes has already started charting the meterwavelengh pulsar sky. Several surveys of the known pulsar population have been conducted over the last few years. The newly upgraded second modification of the Ukrainian T-shaped radio telescope (UTR-2) was utilized to detect 40 pulsars at 10–30 MHz, the lowest radio frequencies available from Earth (Zakharenko et al. 2013). The first station of the Long Wavelength Array (LWA1) was used to measure the flux densities of 44 pulsars at 30–88 MHz (Stovall et al. 2015). At 185 MHz, the Murchison Widefield Array (MWA) was used to detect 50 pulsars (including six millisecond pulsars, Xue et al. 2017) and also to measure flux densities from continuum images (Murphy et al. 2017).

In 2014, we undertook a large campaign of observing almost all known non-recycled radio pulsars with declination, (Dec) Dec > 8° and galactic latitude, (Gb) |Gb| > 3°. The observations were performed with the HBA antennas of the LOFAR telescope at frequencies 110–188 MHz (van Haarlem et al. 2013). The census (hereafter HBA census) encompassed 194 such sources and resulted in 158 detections, updating DMs and measuring flux density values (Bilous et al. 2016, hereafter B16). Based on the measurements at 110–188 MHz and the previously published flux densities, broadband spectra were constructed and the spectral indices were measured with a single or broken power-law models. We demonstrated that the spectra of most pulsars are not well known. Also, regular flux density measurements are needed, as flux densities can typically vary up to an order of magnitude due to diffractive and refractive interstellar scintillation, and/or due to intrinsic variability. With the exception of a handful bright pulsars with hundreds of flux density measurements, the choice of the model and the frequency of the spectral

turnover depends greatly on the poorly explored low-frequency end of the spectrum.

To investigate the shape of the pulsar spectra further, we undertook an LBA extension of the HBA census (hereafter, LBA census), encompassing 88 out of 158 pulsars that have been detected in the HBA census. This paper presents the average profiles, DMs and flux density measurements for those pulsars which were detected.

2. Source selection

For the HBA census, we have selected pulsars from the version 1.51 of the ATNF Pulsar Catalogue[1] which satisfied the following criteria: (a) Dec > 8°; (b) |Gb| > 3°; (c) surface magnetic field strength, $B_{\rm surf} > 10^{10}$ G; (d) position error within half of LOFAR's beam width at the upper edge of the HBA band (130″, van Haarlem et al. 2013); (e) not in a globular cluster. For a more detailed review of the selection criteria we refer the reader to B16.

Ideally, the LBA extension of the HBA census would include all pulsars that had been detected with the high-band antennas, except, perhaps the pulsars with considerable scattering and without any prospects of detecting very strong single pulses. In practice, when this project started, the HBA census was not yet processed and completed and only preliminary detection estimates were available.

Originally, observations with LBAs were planned to be conducted with an incoherent dedispersion scheme. Under this scheme the observing band is split into many narrow channels and interstellar dispersion is only compensated for between channels, but not within the channels themselves. The proposed source sample therefore only included pulsars with sufficiently small intra-channel smearing at 30 MHz, with the exact smearing threshold depending on the preliminary S/N estimates from the HBA census, made without proper radio frequency interference (RFI) excision and without ephemerides updates. We did not exclude sources with considerable scattering in the LBA band hoping to detect strong single pulses.

Before the start of observations with the LBAs, the incoherent dedispersion observing scheme was replaced with a coherent observing scheme, which made the intra-channel smearing criterion obsolete. However, the initial target list for the LBA follow-up remained unchanged. At present, with all HBA observations being processed and analysed (leading to substantial changes in some of the S/N estimates), we can regard the LBA census source sample as being an arbitrary subsample of pulsars detected in the HBA census, with some preference for closer/brighter sources (see Fig. 1).

3. Observations and data reduction

Similarly to the HBA census, each pulsar was observed during one session for either 1000 spin periods, or at least 20 min. Pulsars were observed in June 2014 – May 2015 using the LBAs of the LOFAR core stations in the frequency range of 30–89 MHz. In order to compensate for the refraction in the ionosphere, seven beams were formed around each source (beam 0 on the target and beams 1-6 in a hexagonal grid around beam 0 on the nominal position of the target) at a distance of about 210″, approximately half of the telescope resolution at 60 MHz (412.5″, van Haarlem et al. 2013). The coordinates of the sources were taken

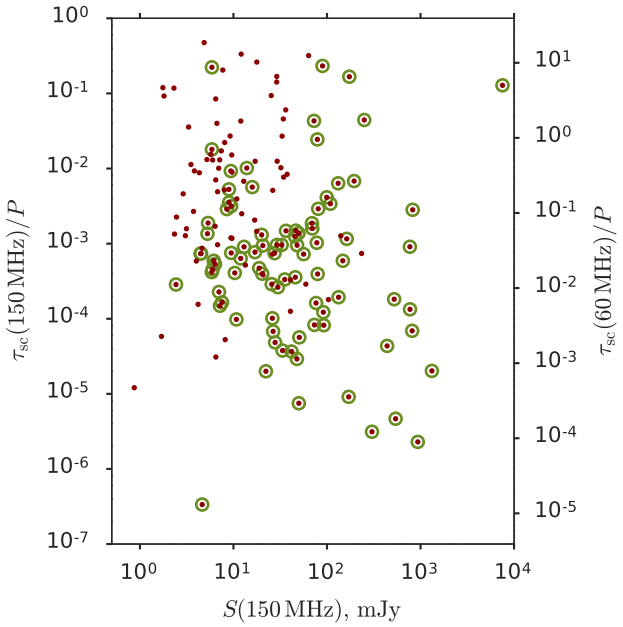

Fig. 1. Band-integrated fluxes and the ratio of scattering time in the middle of the HBA (left y-axis) and LBA (right y-axis) bands to the pulsar spin period for all sources detected in the HBA census (red dots). Green circles mark the pulsars selected for the follow-up with LBAs. The scattering time was estimated with the Galactic electron density model from Yao et al. (2017) and scaled to respective frequencies with an exponent, $\alpha = -4.0$ in $\tau_{\rm sc} \sim \nu^{\alpha}$.

from the ATNF pulsar catalogue, or from the timing observations conducted with the Lovell telescope at Jodrell Bank and the 100-m Robert C. Byrd Green Bank Telescope.

For each beam, the coherently summed complex-voltage signal from individual stations was coherently dedispersed. Raw data were stored in the LOFAR Long-Term Archive[2]. For a more detailed description of LOFAR and its pulsar observing modes, we refer the reader to van Haarlem et al. (2013) and Stappers et al. (2011).

Observations were pre-processed with the standard LOFAR pulsar pipeline (Stappers et al. 2011), which uses the PSRCHIVE software package (Hotan et al. 2004; van Straten et al. 2010). Raw data were converted to full-Stokes samples which were recorded in PSRFITS format (Hotan et al. 2004), with time resolution of 5.12 µs and 300 channels of 195 kHz. Folding produced 5-s sub-integrations with 1024 phase bins. In this paper we focus only on total intensity data. Table B.1 gives the basic observation summary for all pulsars in the LBA sample.

In most cases the raw data were folded using the same ephemerides that were used for folding the HBA census data. Analysis of the HBA census data revealed that in many cases the DM as derived from higher-frequency observations was substantially different from the one obtained from census data. Thus, dedispersing and folding LBA data using incorrect DMs caused substantial pulse smearing within one frequency channel. To mitigate that, we re-dedispersed (coherently) and re-folded 25 pulsars that were affected the most using the DM value obtained in the HBA census. For the remaining pulsars, the smearing was

[1] http://www.atnf.csiro.au/people/pulsar/psrcat/ (Manchester et al. 2005)

[2] http://lofar.target.rug.nl/

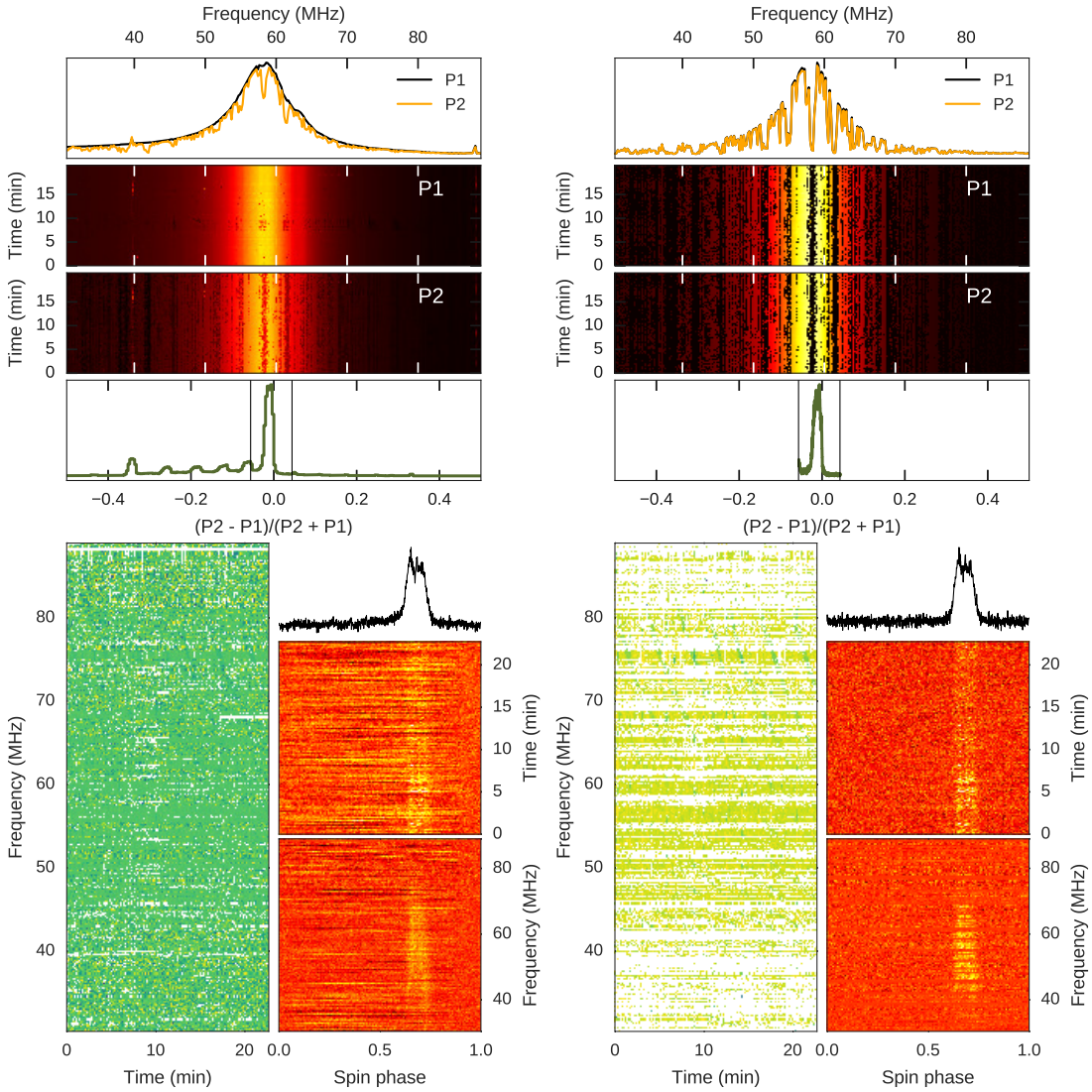

Fig. 2. An example of diagnostic plots without (left) and with (right) dropped packet cleaning applied for one observation of the bright pulsar B0809+74. The upper row of plots shows the statistics of the two polarizations, the lower plots show the dynamic and folded spectra, waterfall diagram, and the average profile.

less than one phase bin at 60 MHz for the downsampled number of bins used in analysis.

After the observations took place it appeared that a substantial fraction of data packets was dropped, resulting in numerous data gaps[3]. These gaps appeared independently in two polarizations and led to significant decrease of overall signal-to-noise ratio (Fig. 2, left). In order to mitigate this adverse effect, we performed an additional step during the RFI cleaning procedure on all data archives. Working with 5-s, 300-channel archives with two polarizations (P1 = XX^* and P2 = YY^*), we computed the histogram of the relative signal strength difference, $dP = (P_2 - P_1)/(P_2 + P_1)$ for each 5-s/195-kHz data cell. We then assigned zero weights to the cells with dP deviating more than by 0.05 from the peak of the histogram (Fig. 2, right).

Since the bandpass in the LBA band is not uniform and has a large peak in sensitivity in the middle of the band, it is necessary to flatten the bandpass before cleaning RFI. Thus, we have divided the dynamic spectrum by an "ideal bandpass", obtained from interpolating the median bandpass from all observations. To remove RFI from the flattened data we used the `clean.py` tool from the `CoastGuard` package (Lazarus et al. 2016).

Archives that were automatically excised of RFI were also visually inspected for residual RFI. In many cases the cleaning procedure was not entirely sufficient, resulting in some relatively faint RFI biasing the baseline estimates for flux calibration. For only three pulsars (namely, PSRs B0105+68, B0643+80, B0656+14), the RFI prevented useful analysis, hence they were excluded from our sample.

Overall, the fraction of band that has been zapped due to dropped packets or RFI is quite substantial, ranging from a few percent to almost the entire band (Table B.1). Zapped fraction varies considerably from beam to beam and is present in most observing runs, not showing a clear dependence on the observing date. While the data used here may not use LOFAR to its full capabilities, and future and ongoing low-frequency observations may reach higher signal-to-noise, the results we present here

[3] The observations were carrying out during the time when new *Cobalt* correlator was put online. But, unfortunately, one of the network switches was misconfigured that resulted in somewhat lower network throughput for the used observing setup that was preliminary tested with the old BG/P beamformer.

still provide useful information about low-frequency end of the pulsar spectra (see Section 4.2).

3.1. Detection and ephemerides update

We adjusted the folding period P and the intra-channel dispersive delay with the PSRCHIVE program `pdmp`, maximizing the integrated S/N of the frequency- and time-averaged profile. Initially, the entire band was used and the diagnostic output from `pdmp` was visually inspected for a pulsar-like signal. For those non-detected in this manner, or the ones with spectra not being visually present across the whole band, we additionally zapped the edges of the band where the sensitivity is low and repeated the search for frequencies between 41 and 78 MHz. To facilitate visual inspection of the average profiles, we downsampled the initial number of phase bins by a factor of 2, 4 or 8.

It is worth mentioning that our DM measurements, based on maximizing S/N of the frequency-integrated profile did not take into account any profile evolution, which usually becomes rapid in the LBA band. Thus, the reported DM values may be subject to a bias depending on the assumed profile evolution model.

Figure 3 shows the correlation between DM and the estimated scattering time over pulsar period for the detected and non-detected pulsars. The same information is also available in Table B.1. Our detections do not extend beyond a DM of $\sim 60\,\mathrm{pc/cm^3}$ and an estimated scattering time fraction of $\sim 20\%$ of the pulse period.

Interestingly enough, one of the pulsars closest to Earth in our sample, J1503+2111, has not been detected. This pulsar had an ostensible error in DM measurements and the HBA census found it at DM $= 3.260 \pm 0.004\,\mathrm{pc/cm^3}$ instead of the previously published DM $= 11.75 \pm 0.06\,\mathrm{pc/cm^3}$ (Champion et al. 2005). The pulsar was subsequently detected in HBAs with the LOFAR French station FR606 at the DM of the HBA census and this DM was used for folding in the current work. Since scattering is unlikely to be at play at this low DM, it is reasonable to assume that in our LBA observations the pulsar has not been detected either because it is intermittent or because its flux density is too low. The upper limit on the band-integrated flux density is ~ 35 mJy (Table B.1), which is comparable with the predicted flux density from the HBA census (~ 20 mJy), so there is no clear indication of the spectral turnover. Note that both the upper limit and the predicted flux density value are subject to large, poorly constrained uncertainties.

3.2. Flux calibration

The folded data files were calibrated in the same way as in the HBA census, thus we refer the reader for the details to B16 and Kondratiev et al. (2016). In short, we have established the flux density scale using the radiometer equation (Dicke 1946), which expresses the noise power through frequency-dependent antenna and sky temperatures, frequency- and direction-dependent telescope gain, observing bandwidth, integration time and the number of polarization summed. The instrument temperature was derived from the measurements of Wijnholds & van Cappellen (2011). The background sky temperature was scaled down to LBA frequencies from 408-MHz maps of Haslam et al. (1982) with the spectral index of −2.55 (Lawson et al. 1987). For the antenna gain, we used the Hamaker model of a station beam (Hamaker 2006) calculated using the `mscorpol`[4] package by Tobia Carozzi. A coherence factor of 0.85 was used to scale the antenna gain with the actual number of stations involved in a given observation (Kondratiev et al. 2016).

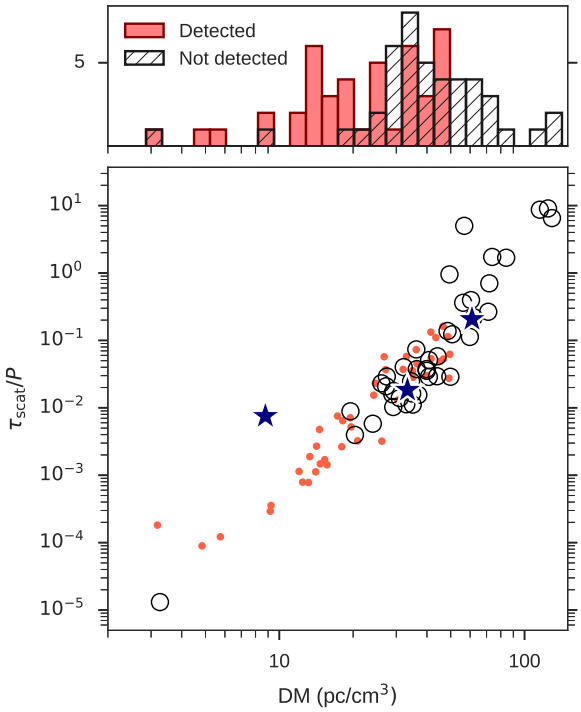

Fig. 3. Detected pulsars (red dots) and the non-detected ones (black circles) versus DM and estimated scattering time at 60 MHz divided by the pulsar period. Scattering times at 1 GHz were taken from the Yao et al. (2017) electron density model and scaled to 60 MHz with an exponent, $\alpha = -4.0$ in $\tau_{sc} \sim \nu^{\alpha}$. Blue stars mark pulsars discarded due to an excess of RFI.

For the Crab pulsar, the sky temperature was complemented with the contribution from the nebula. The latter was estimated with the relation $S_{\mathrm{Jy}} \approx 955\nu_{\mathrm{GHz}}^{-0.27}$ (Bietenholz et al. 1997; Cordes et al. 2004). At 75 MHz, the solid angle occupied by the nebula (radius of 240″, Bietenholz et al. 1997) is smaller than the full-width at the half-maximum of the LOFAR LBA beam (412.5″ van Haarlem et al. 2013), thus the entire nebula is contributing to the system temperature. We must note though that the Crab pulsar is scattered for more than a pulse period in the LBA band, thus the upper limit on the flux density is purely nominal, and, in fact, much smaller than the pulsar point source flux density measurements (B16).

The on- and off-pulse windows for calculating the mean S/N of the pulse profile were selected manually for each pulsar. Calibration was performed in each of 5-s subintegrations and 50 subbands of 11.7 MHz. Zero-weighted sub-bands and/or subintegrations were excluded from calculation of total band width / observing time.

The nominal error on the flux density measurement, $\epsilon_{S\,\mathrm{nom}}$, set by the noise in the off-pulse window does not fully reflect the true flux density measurement uncertainty, since the latter is also influenced by the uncertainties in telescope parameters and scintillation. Since we did not observe any calibrator sources and were limited to only one session per pulsar, we can not estimate those errors separately. The only way to verify our measurements is to compare obtained flux density values to the ones from the literature. For those pulsars for which multiple spectra have been published (e.g. PSRs B0809+74, B1133+16, B1508+55, and others), the LBA measurements are consistent with the re-

[4] `https://github.com/2baOrNot2ba/mscorpol`

ported fluxes, which vary by a factor of a few. More rigorous comparison performed by B16 for the HBA data, based on multiple observing sessions and more numerous literature measurements in the HBA frequency range, suggested adopting 50% of measured flux density as the uncertainty on telescope parameters and scintillation. In this work we extend this uncertainty estimate to the LBA frequency range, deferring thorough study of telescope performance to future work. For our observing setup and pulsar sample, the scintillation-induced flux modulation index, calculated with the basic theory of diffractive and refractive scintillation (Appendix A) is on the order of few percent for the majority of pulsars in the sample (but can be as large as 21%, e.g. for the low-DM pulsar J1503+2111). The total flux density error was calculated by adding the nominal and the 50% errors in quadrature: $\epsilon_S = \sqrt{(0.5S)^2 + \epsilon^2_{S\,\mathrm{nom}}}$.

The mean band-integrated flux densities and their respective uncertainties are listed in Table B.1. For non-detected pulsars we adopted three times the nominal error as the upper limit, although this does not take into account possible signal smearing due to scattering.

Our observing setup involved six beams in a circle surrounding the central beam formed towards the pulsars' coordinates. Interestingly, 19 out of 44 detected pulsars were detected with the highest S/N in a side beam. This is indicative of refraction in the Earth's ionosphere due to differential total electron content (TEC) between the lines-of-sight of different LBA stations. We use the formula for the angular shift due to ionospheric refraction from Loi et al. (2015):

$$|\Delta\theta| = \frac{40.3}{\nu^2}|\nabla_\perp \mathrm{TEC}|. \quad (1)$$

Here the numerical coefficient stems from the combination of fundamental physical constants, the angular shift $\Delta\theta$ is in radians, the transverse gradient of total electron content (along the line of sight in the ionosphere) $\nabla_\perp$TEC is in electrons m^{-3} and ν is in Hz. For the rough estimate of possible values of TEC gradients we used differences in TEC measured by the core HBA LOFAR stations in van Weeren et al. (2016). For δTEC $\sim 10^{14}$ m^{-2} over the core size of 80 km, $\nabla_\perp$TEC is on the order of 10^{11} m^{-2}. At the center of LBA band ($\nu = 60$ MHz) this gives $|\Delta\theta| \sim 230''$ which is comparable to the beam separation. Smaller TEC differences, also reported by van Weeren et al. (2016) will result in smaller refraction angles.

Appendix B shows average profiles, band-integrated or in 2–4 subbands in case of strong pulsars or pulsars with interesting profile evolution.

4. Flux density spectra

4.1. Fitting

For detected pulsars, flux density values were combined with the published measurements (see Table B.1 for the full list of references) and these broadband spectra were fitted with a collection of power law (PL) functions. Similarly to B16, a Bayesian fit was performed in $\lg S - \lg \nu$ space. Each $\lg S$ was modeled as a normally distributed random variable. The mean of the normal distribution was defined by the assumed PL dependence and the standard deviation reflected any kind of intrinsic variability or measurement uncertainty. See B16 for the remarks on PL applicability in general and the choice of a $\lg S$ model in particular.

Depending on the number of flux density measurements, we have approximated $\lg S_{\mathrm{PL}}$ either as a single PL (hereafter "1PL"):

$$\lg S_{1\mathrm{PL}} = \alpha \lg(\nu/\nu_0) + \lg S_0, \quad (2)$$

a broken PL with one break (2PL):

$$\lg S_{2\mathrm{PL}} = \begin{cases} \alpha_{\mathrm{lo}} \lg(\nu/\nu_0) + \lg S_0, & \nu < \nu_{\mathrm{br}} \\ \alpha_{\mathrm{hi}} \lg(\nu/\nu_{\mathrm{br}}) + \alpha_{\mathrm{lo}} \lg(\nu_{\mathrm{br}}/\nu_0) + \lg S_0, & \nu > \nu_{\mathrm{br}}, \end{cases} \quad (3)$$

or a broken PL with two breaks (3PL):

$$\lg S_{3\mathrm{PL}} = \begin{cases} \alpha_{\mathrm{lo}} \lg(\nu/\nu_0) + \lg S_0, & \nu < \nu^{\mathrm{lo}}_{\mathrm{br}} \\ \alpha_{\mathrm{mid}} \lg(\nu/\nu^{\mathrm{lo}}_{\mathrm{br}}) + \alpha_{\mathrm{lo}} \lg(\nu^{\mathrm{lo}}_{\mathrm{br}}/\nu_0) + \lg S_0, & \nu^{\mathrm{lo}}_{\mathrm{br}} < \nu < \nu^{\mathrm{hi}}_{\mathrm{br}} \\ \alpha_{\mathrm{hi}} \lg(\nu/\nu^{\mathrm{hi}}_{\mathrm{br}}) + \alpha_{\mathrm{mid}} \lg(\nu^{\mathrm{hi}}_{\mathrm{br}}/\nu_0) + \lg S_0, & \nu > \nu^{\mathrm{hi}}_{\mathrm{br}}. \end{cases} \quad (4)$$

The reference frequency ν_0 was taken to be close to the geometric average of the minimum and maximum frequencies in the spectrum.

As in B16, for the small number of flux density measurements (treating all measurements within 10% in frequency as a single group), we fixed the uncertainty at the level defined by reported errors. For larger number of frequency groups, an additional fit parameter was introduced, the unknown error $\sigma^{\mathrm{unkn}}_{\lg S}$. A single error per source was fitted, representing intrinsic variability, or any kind of unaccounted propagation or instrumental error. The total flux density uncertainty of any $\lg S$ was then taken as the known and unknown errors added in quadrature.

The posterior distribution of $\sigma^{\mathrm{unkn}}_{\lg S}$ was used to discriminate between models. 1PL was taken as a null hypothesis and rejected in favour of 2PL or 3PL if the latter gave statistically smaller $\sigma^{\mathrm{unkn}}_{\lg S}$. For the details we refer the reader to B16. If no $\sigma^{\mathrm{unkn}}_{\lg S}$ was fitted, we adopted 1PL as the single model. In a few cases, when the data showed a hint of a spectral break, but no $\sigma^{\mathrm{unkn}}_{\lg S}$ was fitted, we fitted 2PL with the break frequency fixed at the frequency of the largest flux density measurement. For such pulsars we give both 1PL and 2PL values of the fitted parameters. Upper limits on flux densities were not taken into account while fitting.

4.2. Results

Seventeen out of the 43 detected pulsars did not have published flux density measurements in the LBA frequency range. Some of them do not show signs of scattering, which indicates an opportunity to study these pulsars at even lower frequencies: for example PSRs B0011+47, B0226+70, and B2022+50 did not exhibit any sign of low-frequency turnover or ostensible scattering down to 40 MHz (see Figures in the Appendix C).

Overall, our new spectral indices are very similar to the ones published in B16. For pulsars with relatively well-measured spectra, the LBA flux densities agree reasonably well with previous measurements in this frequency region. In some cases (e.g. PSRs B0450+55, B0655+64, B2217+47), LBA flux densities are lower by a factor of a few with respect to the measurements of Stovall et al. (2015). However, this is not the case for all LBA census pulsars that overlap with their sample (e.g. PSR B1929+21) and there is at least one example where fluxes from Stovall et al. (2015) are much higher than the bulk of other literature measurements in the same frequency region (PSR B1133+16).

For pulsars with fewer spectral points and no previous measurements below 100 MHz, LBA fluxes did not span enough of the frequency range to have a large influence on the spectral index. For some sources the S/N was sufficient to break the LBA band in two or more subbands and the flux density values hint to a possible spectral break (e.g. PSR J0611+30), however large

errors and close proximity in frequency between the new data points do not make the break statistically significant.

Some of the sources had a different number of PL breaks than in B16 (e.g. PSRs B0450+55, B1133+16, B1811+40, B2217+47). This mostly stems from the influence of separate flux measurements on the fitted $\sigma^{\rm unkn}_{\lg S}$: since we fitted only one unknown error per source. Sometimes the low-frequency (or even high-frequency) breaks were substantially different than in B16 (e.g. PSRs B0823+26, B1530+27, B1737+13).

It is worth mentioning that parallel to this study, a similar census of the pulsar population visible below 100 MHz was undertaken by the LOFAR international station FR606 (Bondonneau et al, submitted). They observed a similar sample of pulsars (103 compared to the 88 pulsars of the present study). The reduced collecting area (∼10%) was compensated by long integrations (on average 3h per target). With this, the authors detected 64 pulsars, compared to the 43 pulsars of the present study. For the detailed comparison of the results, we refer the reader to Bondonneau et al. (submitted).

5. Discussion

Despite its limitations, the LBA extension of the HBA census provides useful information, identifying more than a dozen pulsars for the subsequent follow-up at the lowest frequencies observable from Earth. We provide reference average profiles and fluxes for the 43 pulsars detected, 17 of them having no previously published flux densities at these frequencies.

Overall, the main concerns raised in B16 remain standing: despite being one of the basic characteristics of pulsars, their spectra remain, to a large extent, poorly constrained due to the lack of robust, systematic multifrequency measurements. The situation is even worse at the low-frequency edge, where a spectral break is widely expected.

Proper quantification of the low-frequency spectral break is essential for studying the emission mechanism and propagation of radio waves in the magnetosphere. The existence of low-frequency turnover has been attributed previously to a number of physical processes, for example synchrotron self-absorption (Sieber 1973), refraction of the ordinary radio wave mode (Beskin 2018), free-free absorption (Malov 1979), or stimulated scattering (Lyubarskii & Petrova 1996). In particular, Beskin (2018) proposes clear dependence of the turnover frequency on the pulsar spin period, something that may be readily verified with the future observations. However, such study would require a large number of well-measured spectra from pulsars of substantially different periods. Furthermore, the influence of the ISM on the observed flux densities (for example, decrease in apparent pulsed flux density due to scattering) should be carefully accounted for, for example measuring continuum flux densities at the low radio frequencies (Shimwell et al. 2019).

Future observations of pulsars below 100 MHz can provide more robust flux density measurements and better constrain spectral break(s). This will be achieved, in particular, by the NenuFAR radio telescope (Zarka et al. 2012, 2014, 2015) and its pulsar instrumentation LUPPI (Bondonneau et al. 2019), with which we are currently conducting a systematic census of the pulsar population (Bondonneau et al. in prep). Due to its sensitivity, its constant antenna response across its frequency band (10–85 MHz), and long integrations, it is expected that NenuFAR will detect a much larger number of pulsars compared to the LBA census and its companion study with FR606.

Acknowledgements. This works makes extensive use of `matplotlib`[5] (Hunter 2007), `seaborn`[6] Python plotting libraries and NASA's Astrophysics Data System. This paper is based on data obtained with the International LOFAR Telescope (ILT) under project code `LC2_025`. LOFAR (van Haarlem et al. 2013) is the Low Frequency Array designed and constructed by ASTRON. It has observing, data processing, and data storage facilities in several countries, that are owned by various parties (each with their own funding sources), and that are collectively operated by the ILT foundation under a joint scientific policy. The ILT resources have benefited from the following recent major funding sources: CNRS-INSU, Observatoire de Paris and Université d'Orléans, France; BMBF, MIWF-NRW, MPG, Germany; Science Foundation Ireland (SFI), Department of Business, Enterprise and Innovation (DBEI), Ireland; NWO, The Netherlands; The Science and Technology Facilities Council, UK.

Appendix A: Scintillation

The variation of observed flux due to scintillation on the inhomogeneities in the interstellar medium was estimated with a simple thin-screen Kolmogorov model (see Lorimer & Kramer 2005, for review). The scintillation bandwidth was taken to be $\Delta f = 1.16/(2\pi\tau_{\rm scat}) \times (60\,{\rm MHz}/1\,{\rm GHz})^{4.0}$, where $\tau_{\rm scat}$ is scattering time at 1 GHz from Yao et al. (2017). For all census pulsars the scintillation bandwidth Δf was smaller than a few kHz, satisfying the conditions of strong scintillation regime ($\sqrt{f/\Delta f} > 1$).

Diffractive interstellar scintillation (DISS) did not have a large impact on the flux variation since many scintles were averaged in the frequency domain, resulting in modulation index $m_{\rm DISS}$ (rms of the flux density divided by its mean value) was on the order of a percent or less. The refractive scintillation (RISS) was much stronger with typical $m_{\rm RISS} \approx 0.05 - 0.1$. Table B.1 lists the expected values of total modulation index.

Appendix B: Tables

Table B.1 summarizes observations. The columns indicate: pulsar name; approximate spin period (s); observing epoch (MJD); duration of an observing session (min); frequency range (MHz); best beam (usually the one with highest S/N); fraction of zapped data in the dynamic spectrum for the least and the most affected beams; peak S/N of the average profile; DM from B16; measured census DM; expected Yao et al. (2017) scattering time at 60 MHz divided by pulsar period; expected modulation index due to scintillation in the ISM; mean flux density within specified frequency range (upper limit for the non-detected pulsars), and the literature references to previous flux density measurements. The values in parentheses indicate the errors on the last two significant digits.

Tables B.2–B.4 contain best fitted parameters for the pulsars with the spectra modelled with a single PL, a PL with one break and a PL with two breaks, respectively. The columns include pulsar name; spectral frequency span (MHz); number of data points in spectrum, N_p; the reference frequency, ν_0 (MHz); flux density at the reference frequency, S_0 (mJy); spectral index (or indices in case of broken PLs), α; and fitted flux density scatter, $\sigma^{\rm unkn}_{\lg S}$, if applicable (see Sect. 4.1). Tables B.3 and B.4 also include break frequency, $\nu_{\rm br}$ (MHz), together with its 68% uncertainty range.

[5] `http://matplotlib.org/`
[6] `http://stanford.edu/~mwaskom/software/seaborn/`

Table B.1. Observation summary, DM and flux density measurements.

PSR	Period P (s)	Observing epoch (MJD)	Obs. time (min)	Freq. range (MHz)	Best beam	Zapped fraction	Peak S/N	DM_{cen} (pc cm^{-3})	Expected τ_{scat}/P	Exp. mod. index	Mean flux (mJy)	Literature flux references
B0011+47	1.241	56949.82	21	42.12–76.15	0	0.21–0.43	6	30.3048 (65)	1e-02	0.08	45 ± 25	3, 15, 19, 22, 25, 38, 42, 46, 57
B0045+33	1.217	57112.46	21	42.35–77.09	...	0.45–0.55	...	...	4e-02	0.06	<56.0	3, 16, 38, 46, 49, 57, 64
B0052+51	2.115	57114.46	36	42.10–77.23	...	0.16–0.17	...	...	3e-02	0.06	<22.6	3, 16, 19, 25, 38, 46, 49
B0053+47	0.472	57027.69	20	30.37–77.24	5	0.05–0.06	15	18.0954 (10)	6e-03	0.10	110 ± 60	3, 16, 28, 38, 49, 64, 69
B0105+68[♯]	1.071	57148.40	20	42.05–77.24	...	0.81–0.85	...	...	2e-01	0.05	<140.7	3, 16, 38, 49, 57, 64
B0114+58	0.101	57112.48	20	42.41–77.19	...	0.48–0.63	...	...	1e+00	0.06	<99.8	3, 19, 35, 38, 49, 60
J0137+1654	0.415	56827.22	20	42.15–77.29	...	0.17–0.35	...	...	2e-02	0.08	<42.8	3, 37, 69
B0136+57	0.272	56827.28	20	42.15–77.19	...	0.26–0.45	...	...	2e+00	0.04	<47.8	3, 15, 22, 25, 38, 46, 49, 56, 57
B0153+39	1.811	56827.24	31	42.14–77.13	...	0.32–0.59	...	...	1e-01	0.05	<52.6	3, 16, 19, 38, 49, 64
B0226+70	1.467	56827.26	25	42.26–77.05	0	0.22–0.36	7	46.7394 (66)	5e-02	0.06	49 ± 29	3, 16, 38, 42, 46, 49, 57, 64
B0301+19	1.388	56975.00	24	42.13–77.13	0	0.28–0.57	10	15.6568 (99)	1e-03	0.11	61 ± 33	3, 17, 21, 22, 25, 28, 38, 42, 46, 47, 48, 49, 56, 57, 59, 69
B0320+39	3.032	56903.21	65	42.08–77.29	3	0.38–0.41	29	26.1698 (20)	3e-03	0.08	76 ± 39	3, 15, 17, 22, 28, 29, 38, 42, 46, 57, 59, 69
J0324+5239	0.337	56903.25	20	42.16–77.18	...	0.28–0.54	...	...	9e+00	0.03	<70.5	2, 3
B0410+69	0.391	56975.03	20	42.18–77.29	...	0.17–0.47	...	...	3e-02	0.08	<38.4	3, 16, 19, 28, 38, 49, 57, 69
J0417+35	0.654	56975.02	20	42.08–77.26	...	0.21–0.52	...	...	1e-01	0.06	<38.0	3, 9, 49
B0450+55	0.341	56903.26	20	42.23–76.93	0	0.31–0.53	12	14.590 (77)	5e-03	0.11	110 ± 60	3, 25, 38, 46, 49, 50, 57, 59, 61, 69
B0531+21	0.034	56903.27	20	41.89–77.28	...	0.45–0.53	...	...	5e+00	0.05	<70.6	1, 3, 28, 38, 40, 42, 44, 48, 49, 50, 53, 57
J0611+30	1.412	56975.08	24	42.13–77.22	0	0.19–0.49	8	45.2951 (81)	5e-02	0.06	89 ± 46	3, 9
B0609+37	0.298	56975.07	20	42.10–77.22	4	0.15–0.41	6	27.175 (49)	4e-02	0.08	46 ± 25	3, 28, 38, 46, 49, 57, 60, 69
B0626+24	0.476	56903.29	20	42.04–77.24	...	0.56–0.64	...	...	2e+00	0.04	<51.5	3, 15, 17, 25, 28, 38, 46, 49, 50, 57
B0643+80[♯]	1.215	56903.34	21	42.17–77.09	...	0.68–0.79	...	...	2e-02	0.07	<66.8	3, 28, 38, 42, 49, 57
B0655+64	0.196	56903.32	20	42.29–77.23	0	0.60–0.67	14	8.7739 (19)	2e-03	0.14	86 ± 49	3, 15, 38, 41, 57, 59, 61, 69
B0656+14[♯]	0.385	56903.33	20	42.06–77.06	...	0.82–0.98	...	...	4e-03	0.11	<94.8	3, 22, 23, 24, 38, 46, 47, 49, 57, 65, 69, 70
B0751+32	1.442	56975.11	25	42.09–77.35	4	0.19–0.50	4	39.846 (84)	3e-02	0.06	21 ± 13	3, 15, 22, 28, 38, 49, 57
B0809+74	1.292	56903.37	22	30.64–77.17	3	0.55–0.68	34	5.7707 (84)	1e-04	0.17	1400 ± 700	3, 6, 13, 21, 22, 25, 28, 29, 31, 34, 38, 42, 43, 46, 48, 49, 50, 57, 61, 69
B0823+26	0.531	56975.12	20	30.37–77.19	4	0.16–0.44	107	19.4763 (35)	7e-03	0.10	700 ± 350	3, 5, 6, 10, 14, 18, 21, 22, 25, 29, 33, 35, 37, 38, 42, 43, 45, 46, 48, 49, 50, 57, 59, 61, 66, 67, 69
B0841+80	1.602	56975.14	27	42.33–77.18	...	0.19–0.49	...	...	2e-02	0.07	<24.5	3, 16, 19, 49, 57, 64
B0917+63	1.568	56975.16	27	42.09–77.34	0	0.21–0.51	13	13.1542 (42)	8e-04	0.12	41 ± 22	3, 16, 19, 38, 49, 64, 69
B0940+16	1.087	56903.40	20	42.01–77.19	...	0.64–0.74	...	...	4e-03	0.10	<61.2	3, 17, 22, 24, 37, 38, 47, 57, 65, 69
J0943+22	0.533	56903.39	20	42.08–77.53	...	0.52–0.64	...	...	2e-02	0.08	<39.2	3, 49, 63
B0943+10	1.098	56826.71	20	30.40–77.17	0	0.16–0.36	50	15.3585 (72)	2e-03	0.11	400 ± 200	3, 13, 22, 38, 42, 48, 49, 50, 52, 57, 61, 69
J0947+27	0.851	57109.86	20	42.11–77.23	...	0.07–0.09	...	...	2e-02	0.08	<19.7	3, 54, 69
B1112+50	1.656	57028.15	28	30.37–77.24	0	0.07–0.10	26	9.1863 (11)	3e-04	0.14	43 ± 22	3, 21, 22, 32, 38, 42, 43, 46, 48, 49, 50, 57, 59, 69
B1133+16	1.188	56826.74	20	30.39–77.21	4	0.17–0.27	135	4.8407 (78)	9e-05	0.18	880 ± 440	3, 5, 6, 10, 13, 14, 18, 21, 22, 23, 24, 25, 29, 31, 30, 32, 33, 34, 35, 38, 42, 43, 46, 47, 48, 49, 50, 57, 59, 61, 62, 66, 68, 69, 70
J1238+21	1.119	56826.80	20	42.11–77.26	4	0.14–0.17	18	17.9706 (79)	3e-03	0.10	37 ± 20	3, 49, 54, 69

Continued on next page

Table B.1 – *Continued from previous page*

PSR	Period P (s)	Observing epoch (MJD)	Obs. time (min)	Freq. range (MHz)	Best beam	Zapped fraction	Peak S/N	DM_{cen} (pc cm^{-3})	Expected τ_{scat}/P	Exp. mod. index	Mean flux (mJy)	Literature flux references
B1237+25	1.383	56826.76	24	42.11–77.25	4	0.08–0.12	61	9.2716 (90)	4e-04	0.14	150 ± 80	3, 5, 6, 10, 17, 18, 21, 22, 25, 29, 31, 38, 42, 43, 46, 48, 49, 50, 57, 59, 61, 62, 69, 70
J1313+0931	0.849	56826.79	20	42.25–76.00	4	0.19–0.39	6	12.0406 (15)	1e-03	0.12	24 ± 19	3, 39, 69
B1322+83	0.670	57007.33	20	42.19–77.17	3	0.20–0.22	5	13.2962 (30)	2e-03	0.12	20 ± 13	3, 19, 28, 38, 42, 49, 50, 64, 69
J1503+2111	3.314	56826.82	81	42.18–77.27	…	0.54–0.67	…	…	1e-05	0.21	<35.9	3, 7, 19, 69
B1508+55	0.740	56826.86	20	30.26–77.34	4	0.21–0.45	82	19.6189 (48)	5e-03	0.10	390 ± 190	3, 5, 18, 21, 22, 25, 29, 31, 34, 38, 42, 43, 46, 48, 49, 56, 57, 59, 61, 69
B1530+27	1.125	57007.39	20	42.13–77.22	0	0.20–0.22	24	14.711 (28)	1e-03	0.11	78 ± 40	3, 15, 37, 38, 41, 42, 46, 49, 57, 69
B1541+09	0.748	56826.89	20	42.20–77.15	4	0.18–0.38	8	34.9958 (46)	4e-02	0.07	310 ± 160	3, 21, 22, 28, 38, 42, 43, 46, 47, 48, 49, 50, 56, 57, 59, 61
J1549+2113	1.263	56913.72	22	42.29–77.10	…	0.55–0.73	…	…	6e-03	0.09	<91.8	3, 19, 37, 49, 69
J1612+2008	0.427	56826.95	20	42.16–77.23	…	0.17–0.34	…	…	9e-03	0.10	<55.1	3, 4
J1627+1419	0.491	56826.91	20	42.11–77.21	…	0.12–0.22	…	…	4e-02	0.07	<68.0	3, 19, 36, 49
B1633+24	0.491	56949.66	20	42.20–77.43	5	0.41–0.62	6	24.2471 (24)	2e-02	0.09	72 ± 41	3, 38, 49, 50, 57, 64, 65, 69
J1645+1012	0.411	56826.93	20	42.17–77.19	3	0.15–0.34	4	36.171 (16)	7e-02	0.07	64 ± 39	3, 36, 49
J1649+2533	1.015	56949.68	20	41.97–77.42	…	0.47–0.71	…	…	2e-02	0.07	<68.8	3, 19, 36, 49
J1652+2651	0.916	57107.21	20	42.10–77.23	…	0.05–0.07	…	…	5e-02	0.06	<31.9	3, 19, 36, 37, 49, 58
J1720+2150	1.616	56913.74	27	42.57–77.12	…	0.41–0.60	…	…	3e-02	0.06	<57.6	3, 19, 36, 49
B1737+13	0.803	56826.96	20	42.06–77.23	2	0.19–0.44	19	48.6682 (11)	1e-01	0.06	87 ± 47	3, 25, 28, 38, 46, 47, 49, 50, 56, 57
J1741+2758	1.361	56949.69	23	43.16–77.19	…	0.50–0.77	…	…	1e-02	0.08	<56.3	3, 19, 36, 49, 69
J1746+2245	3.465	57125.14	69	42.09–77.24	…	0.29–0.29	…	…	3e-02	0.06	<21.6	3, 7, 19
J1752+2359	0.409	56949.71	20	42.21–77.31	…	0.29–0.46	…	…	7e-02	0.07	<51.3	3, 36, 49
B1753+52	2.391	57107.23	40	42.11–77.23	…	0.09–0.11	…	…	1e-02	0.07	<19.1	3, 16, 19, 28, 38, 49
J1758+3030	0.947	56949.72	20	50.20–77.32	5	0.36–0.65	5	35.1074 (28)	3e-02	0.07	44 ± 31	3, 9, 19, 49, 58
B1811+40	0.931	56899.88	20	42.17–77.17	0	0.28–0.45	6	41.5766 (52)	5e-02	0.06	36 ± 22	3, 11, 15, 22, 28, 38, 41, 50, 57
J1838+1650	1.902	56949.74	32	41.89–77.38	…	0.52–0.84	…	…	1e-02	0.07	<92.5	3, 19, 37
B1839+09	0.381	56826.98	20	42.21–77.26	0	0.17–0.34	5	49.1779 (54)	2e-01	0.06	190 ± 100	3, 25, 28, 38, 41, 46, 47, 50, 57
B1839+56	1.653	56826.99	28	30.37–77.24	0	0.07–0.08	166	26.7916 (11)	6e-03	0.08	440 ± 220	3, 22, 25, 34, 38, 42, 46, 49, 50, 57, 59, 61, 69
B1842+14	0.375	56827.01	20	42.20–77.20	0	0.26–0.46	32	41.5056 (46)	1e-01	0.06	830 ± 420	3, 22, 38, 42, 46, 47, 50, 55, 57, 59
J1900+30	0.602	56899.89	20	42.26–77.46	…	0.19–0.37	…	…	7e-01	0.04	<48.7	3, 9
B1905+39	1.236	57006.53	21	42.22–77.26	…	0.27–0.36	…	…	1e-02	0.08	<35.3	3, 15, 22, 28, 38, 46, 57
B1919+21	1.337	56827.03	23	30.38–77.23	0	0.12–0.14	453	12.444 (87)	8e-04	0.12	4600 ± 2300	3, 5, 12, 13, 17, 18, 21, 22, 31, 34, 38, 42, 43, 46, 48, 49, 55, 57, 59, 61, 68, 69
B1929+10	0.227	56827.04	20	30.40–77.12	0	0.17–0.34	28	3.1832 (34)	2e-04	0.22	950 ± 480	3, 5, 6, 10, 12, 14, 18, 19, 20, 22, 25, 27, 29, 33, 35, 37, 38, 42, 43, 46, 47, 48, 49, 50, 55, 57, 62, 67, 68, 69, 70
B1946+35	0.717	56827.06	20	42.18–77.23	…	0.12–0.23	…	…	7e+00	0.03	<79.5	3, 12, 17, 25, 38, 42, 43, 46, 49, 52, 55, 57, 70
B1953+50	0.519	57006.52	20	42.05–77.27	0	0.19–0.26	4	31.9827 (53)	4e-02	0.07	22 ± 17	3, 15, 22, 38, 41, 46, 49, 57
J2017+2043	0.537	57126.25	20	42.10–77.25	…	0.06–0.10	…	…	4e-01	0.05	<43.1	3, 19, 51
B2016+28	0.558	56827.10	20	30.38–77.25	0	0.12–0.23	38	14.2239 (36)	3e-03	0.11	490 ± 250	3, 5, 6, 10, 12, 21, 22, 28, 29, 38, 43, 46, 48, 49, 50, 55, 56, 57, 59, 61, 68, 69
B2020+28	0.343	56827.08	20	42.09–77.21	0	0.25–0.49	16	24.6311 (40)	2e-02	0.09	120 ± 60	3, 5, 6, 12, 21, 22, 29, 33, 35, 38, 43, 46, 48, 49, 50, 55, 56, 57, 59, 62, 66, 67, 68, 69
B2022+50	0.373	57006.66	20	42.09–77.24	5	0.08–0.10	6	33.0282 (50)	6e-02	0.07	69 ± 38	3, 16, 19, 35, 38, 46, 49, 57

Continued on next page

Table B.1 – *Continued from previous page*

PSR	Period P (s)	Observing epoch (MJD)	Obs. time (min)	Freq. range (MHz)	Best beam	Zapped fraction	Peak S/N	DM_{cen} (pc cm^{-3})	Expected τ_{scat}/P	Exp. mod. index	Mean flux (mJy)	Literature flux references
B2034+19	2.074	57126.27	35	42.12–77.25	...	0.07–0.12	...	...	2e-02	0.07	<25.7	3, 60
J2040+1657	0.866	57006.60	20	42.04–77.33	...	0.12–0.17	...	...	1e-01	0.06	<36.7	3, 37
B2044+15	1.138	56949.76	20	42.27–77.11	...	0.30–0.45	...	...	4e-02	0.06	<48.1	3, 22, 28, 38, 42, 46, 47
B2053+21	0.815	57126.29	20	42.10–77.24	...	0.04–0.06	...	...	4e-02	0.07	<34.2	3, 38, 42, 46, 60
B2113+14	0.440	56827.12	20	42.18–77.19	...	0.15–0.34	...	...	4e-01	0.05	<46.0	3, 38, 41, 42, 47, 50, 57, 65
J2139+2242	1.083	57126.30	20	42.10–77.25	...	0.06–0.11	...	...	6e-02	0.06	<39.0	3, 19, 49, 58
B2154+40	1.525	56827.14	26	42.09–77.28	...	0.25–0.50	...	...	3e-01	0.04	<45.2	3, 21, 22, 25, 28, 29, 38, 43, 46, 49, 50, 56, 57
B2217+47	0.538	56827.16	20	30.32–77.24	0	0.22–0.47	62	43.5062 (35)	1e-01	0.06	1300 ± 600	3, 10, 12, 17, 21, 22, 25, 34, 38, 43, 48, 49, 56, 57, 59, 61, 64
B2224+65	0.683	56949.78	20	42.02–77.37	6	0.37–0.59	25	36.5036 (17)	5e-02	0.07	370 ± 180	3, 12, 21, 22, 25, 29, 38, 42, 43, 46, 50, 57, 61
B2227+61	0.443	56949.79	20	42.01–77.23	...	0.22–0.39	...	...	9e+00	0.03	<60.5	3, 38, 49, 50, 57
J2253+1516	0.792	56899.91	20	42.26–77.25	...	0.16–0.30	...	...	2e-02	0.08	<42.5	3, 8, 19, 49, 69
B2303+30	1.576	56899.94	27	42.22–77.32	0	0.30–0.56	5	49.6445 (50)	6e-02	0.06	27 ± 21	3, 21, 22, 28, 37, 38, 43, 50, 55, 57, 59
B2303+46	1.066	56949.81	20	42.23–77.15	...	0.29–0.49	...	...	2e-01	0.05	<44.5	3, 16, 19, 26, 38, 49
B2306+55	0.475	56899.93	20	42.14–77.17	0	0.11–0.16	7	46.559 (71)	2e-01	0.06	180 ± 90	3, 12, 17, 22, 38, 46, 50, 57
B2310+42	0.349	56827.19	20	42.12–77.12	0	0.12–0.25	8	17.2969 (19)	8e-03	0.10	66 ± 35	3, 5, 15, 17, 18, 22, 28, 38, 42, 46, 49, 50, 57, 69
B2315+21	1.445	56827.20	25	30.37–77.06	0	0.25–0.44	18	20.8896 (94)	3e-03	0.09	33 ± 19	3, 15, 22, 28, 37, 38, 46, 49, 50, 57, 69

References. [1] Bridle (1970); [2] Barr et al. (2013); [3] Bilous et al. (2016); [4] Boyles et al. (2013); [5] Bhat et al. (1999); [6] Bartel et al. (1978); [7] Champion et al. (2005); [8] Camilo & Nice (1995); [9] Camilo et al. (1996); [10] Downs (1979); [11] Dembska et al. (2014); [12] Davies et al. (1977); [13] Deshpande & Radhakrishnan (1992); [14] Downs et al. (1973); [15] Damashek et al. (1978); [16] Dewey et al. (1985); [17] Fomalont et al. (1992); [18] Gould (1994); [19] Han et al. (2009); [20] Hobbs et al. (2004); [21] Izvekova et al. (1979); [22] Izvekova et al. (1981); [23] Johnston et al. (2006); [24] Jankowski et al. (2018); [25] Kaplan et al. (1998); [26] Kijak et al. (2007); [27] Kramer et al. (1997); [28] Kijak et al. (1998); [29] Kuzmin et al. (1986); [30] Krzeszowski et al. (2014); [31] Kuz'min et al. (1978); [32] Karuppusamy et al. (2011); [33] Kramer et al. (1996); [34] Lane et al. (2014); [35] Löhmer et al. (2008); [36] Lewandowski et al. (2004); [37] Lorimer et al. (2005); [38] Lorimer et al. (1995); [39] Lommen et al. (2000); [40] Manchester (1971); [41] Malofeev (1993); [42] Malofeev (1999); [43] Morris et al. (1981); [44] Moffett & Hankins (1999); [45] Murphy et al. (2017); [46] Maron et al. (2000); [47] Manchester et al. (1978); [48] Malofeev & Malov (1980); [49] Malofeev et al. (2000); [50] Manchester & Taylor (1981); [51] Navarro et al. (2003); [52] Rankin & Benson (1981); [53] Rankin et al. (1970); [54] Ray et al. (1996); [55] Slee et al. (1986); [56] Stinebring & Condon (1990); [57] Seiradakis et al. (1995); [58] Sayer et al. (1997); [59] Stovall et al. (2015); [60] Stokes et al. (1986); [61] Shrauner et al. (1998); [62] Sieber & Wielebinski (1987); [63] Thorsett et al. (1993); [64] Taylor et al. (2000); [65] Vivekanand et al. (1983); [66] Wielebinski et al. (1993); [67] Wang et al. (2005); [68] Xue et al. (2017); [69] Zakharenko et al. (2013); [70] Zhao et al. (2017).

Notes. (♯) PSRs B0105+68, B0643+80, B0656+14 were excluded from analysis because of RFI contamination.

Table B.2. Fit results for pulsars with a single PL spectrum.

PSR	Frequency span (MHz)	# of points, N_p	Ref. freq., ν_0 (MHz)	Ref. flux, S_0 (mJy)	Spectral index, α	Fitted flux scatter, $\sigma^{unkn}_{\lg S}$	PSR	Frequency span (MHz)	# of points, N_p	Ref. freq., ν_0 (MHz)	Ref. flux, S_0 (mJy)	Spectral index, α	Fitted flux scatter, $\sigma^{unkn}_{\lg S}$
B0011+47	59 – 4850	19	500	11.0	-0.9 ± 0.1	0.11	J1238+21♯	25 – 430	6	100	22.0	-0.8 ± 0.3	...
B0053+47	20 – 4850	10	300	4.7	-1.3 ± 0.2	0.43	J1313+0931♯	59 – 1400	4	300	6.2	-2.3 ± 0.3	...
B0226+70	59 – 1420	10	300	3.8	-1.6 ± 0.2	0.08	J1645+1012♯	59 – 430	4	200	14.0	-2.1 ± 0.4	...
J0611+30♯	45 – 430	4	100	38.0	-1.9 ± 0.4	...	J1758+3030	59 – 800	9	200	20.0	-1.4 ± 0.3	0.11
B0609+37	59 – 4850	13	500	5.2	-1.4 ± 0.2	0.30	B1842+14	47 – 4850	21	500	14.0	-1.95 ± 0.09	0.05
B0655+64	45 – 1408	15	300	14.0	-2.0 ± 0.2	0.34	B1953+50	59 – 4850	13	500	17.0	-1.2 ± 0.1	0.08
B0751+32	59 – 4850	10	500	4.4	-1.4 ± 0.2	0.13	B2022+50	59 – 32000	15	1400	1.9	-1.10 ± 0.08	0.07
B0917+63	45 – 1408	10	300	6.3	-1.4 ± 0.2	0.07	B2224+65	45 – 10700	26	700	7.7	-1.62 ± 0.07	0.07

Notes. (♯) These pulsars have also broken PL fit, with break frequency fixed at the frequency of the largest measured flux density. See Table B.3 for the values of fitted parameters.

Table B.3. Fit results for pulsars where the spectrum was modelled with a broken PL.

PSR	Frequency span (MHz)	# of points, N_p	Ref. freq., ν_0 (MHz)	Ref. flux, S_0 (mJy)	Spectral index, $\alpha_{\rm lo}$	Break freq., $\nu_{\rm br}$ (MHz)	Uncertainty range for $\nu_{\rm br}$ (MHz)	Spectral index, $\alpha_{\rm hi}$	Fitted flux scatter, $\sigma^{\rm unkn}_{\lg S}$
B0301+19	59 – 4850	35	500	24.0	−0.5 ± 0.2	500	354 – 761	−1.9 ± 0.3	0.11
B0320+39	25 – 4850	26	300	52.0	0.9 ± 0.5	157	133 – 195	−2.4 ± 0.2	0.10
J0611+30	45 – 430	4	100	70.0	1.4 ± 1.5	74	…	−2.5 ± 0.5	…
B0809+74	12 – 14800	69	400	110.0	0.8 ± 0.3	66	58 – 73	−1.66 ± 0.06	0.14
B0943+10	20 – 1400	35	200	83.0	0.2 ± 0.6	114	87 – 167	−2.8 ± 0.7	0.31
B1112+50	20 – 4900	37	300	45.0	1.1 ± 0.4	148	133 – 172	−2.3 ± 0.2	0.36
B1133+16	16 – 32000	130	700	100.0	0.1 ± 0.1	232	212 – 257	−1.93 ± 0.06	0.17
J1238+21	25 – 430	6	100	64.0	0.8 ± 0.5	102	…	−2.4 ± 0.4	…
J1313+0931	59 – 1400	4	300	8.6	0.9 ± 1.3	149	…	−2.6 ± 0.3	…
B1322+83	25 – 1408	12	200	59.0	0.8 ± 0.6	214	173 – 306	−2.5 ± 0.6	0.18
B1508+55	20 – 10750	59	500	52.0	2.4 ± 0.4	88	82 – 97	−2.04 ± 0.08	0.14
B1530+27	25 – 4850	22	300	17.0	1.3 ± 0.5	92	74 – 100	−1.6 ± 0.1	0.05
B1541+09	39 – 10550	49	600	29.0	0.7 ± 0.4	144	133 – 156	−2.15 ± 0.09	0.09
B1633+24	25 – 1400	12	200	44.0	0.6 ± 0.5	155	131 – 191	−2.3 ± 0.3	0.06
J1645+1012	59 – 430	4	200	21.0	1.5 ± 1.7	102	…	−2.9 ± 0.5	…
B1737+13	45 – 4850	18	500	20.0	−0.6 ± 0.5	330	153 – 556	−1.7 ± 0.2	0.04
B1839+09	59 – 4850	13	500	14.0	−0.6 ± 0.8	229	135 – 294	−1.9 ± 0.2	0.06
B1839+56	20 – 4850	30	300	32.0	4.8 ± 1.4	39	35 – 41	−1.6 ± 0.1	0.23
B1919+21	16 – 4850	92	300	250.0	0.4 ± 0.2	135	120 – 149	−2.7 ± 0.1	0.21
B1929+10	20 – 43000	98	900	110.0	0.3 ± 0.4	342	240 – 511	−1.74 ± 0.09	0.23
B2016+28	25 – 10700	55	500	150.0	0.1 ± 0.2	331	293 – 379	−2.27 ± 0.09	0.13
B2020+28	45 – 32000	47	1200	24.0	0.6 ± 0.6	307	225 – 430	−1.6 ± 0.1	0.21
B2306+55	59 – 4850	13	500	15.0	−0.7 ± 0.5	357	178 – 532	−2.0 ± 0.2	0.07
B2310+42	25 – 10700	34	500	130.0	0.1 ± 0.3	645	498 – 909	−2.1 ± 0.3	0.18
B2315+21	25 – 4850	16	400	17.0	0.6 ± 0.5	186	167 – 231	−2.1 ± 0.2	0.06

Table B.4. Fit results for pulsars where the spectrum was modelled by a PL with two breaks.

PSR	Frequency span (MHz)	# of points, N_p	Ref. freq., ν_0 (MHz)	Ref. flux, S_0 (mJy)	Spectral index, $\alpha_{\rm lo}$	Lower break freq., $\nu^{\rm lo}_{\rm br}$ (MHz)	Uncertainty range for $\nu^{\rm lo}_{\rm br}$ (MHz)	Spectral index $\alpha_{\rm mid}$	Higher break freq., $\nu^{\rm hi}_{\rm br}$ (MHz)	Uncertainty range for $\nu^{\rm hi}_{\rm br}$ (MHz)	Spectral index, $\alpha_{\rm hi}$	Fitted flux scatter, $\sigma^{\rm unkn}_{\lg S}$
B0450+55	25 – 14600	24	600	30.0	0.5 ± 1.4	94	45 – 243	−1.3 ± 0.5	1914	708 – 4676	−1.8 ± 0.7	0.31
B0823+26	20 – 32000	86	800	39.0	2.0 ± 0.8	54	45 – 65	−1.25 ± 0.08	2808	1199 – 4182	−2.2 ± 0.3	0.08
B1237+25	20 – 24620	82	700	48.0	2.6 ± 1.4	55	36 – 69	−0.9 ± 0.2	843	709 – 917	−2.2 ± 0.1	0.13
B1811+40	59 – 2600	12	400	10.0	−0.9 ± 0.6	260	130 – 413	−1.4 ± 0.6	956	711 – 1060	−2.8 ± 0.6	0.06
B2217+47	35 – 4900	39	400	110.0	−1.0 ± 0.4	241	147 – 357	−2.7 ± 0.6	1257	711 – 1574	−1.8 ± 0.8	0.20
B2303+30	49 – 4850	19	500	14.0	−0.5 ± 0.4	337	236 – 418	−2.7 ± 0.6	928	726 – 1057	−1.2 ± 0.4	0.06

Appendix C: Profiles and spectra

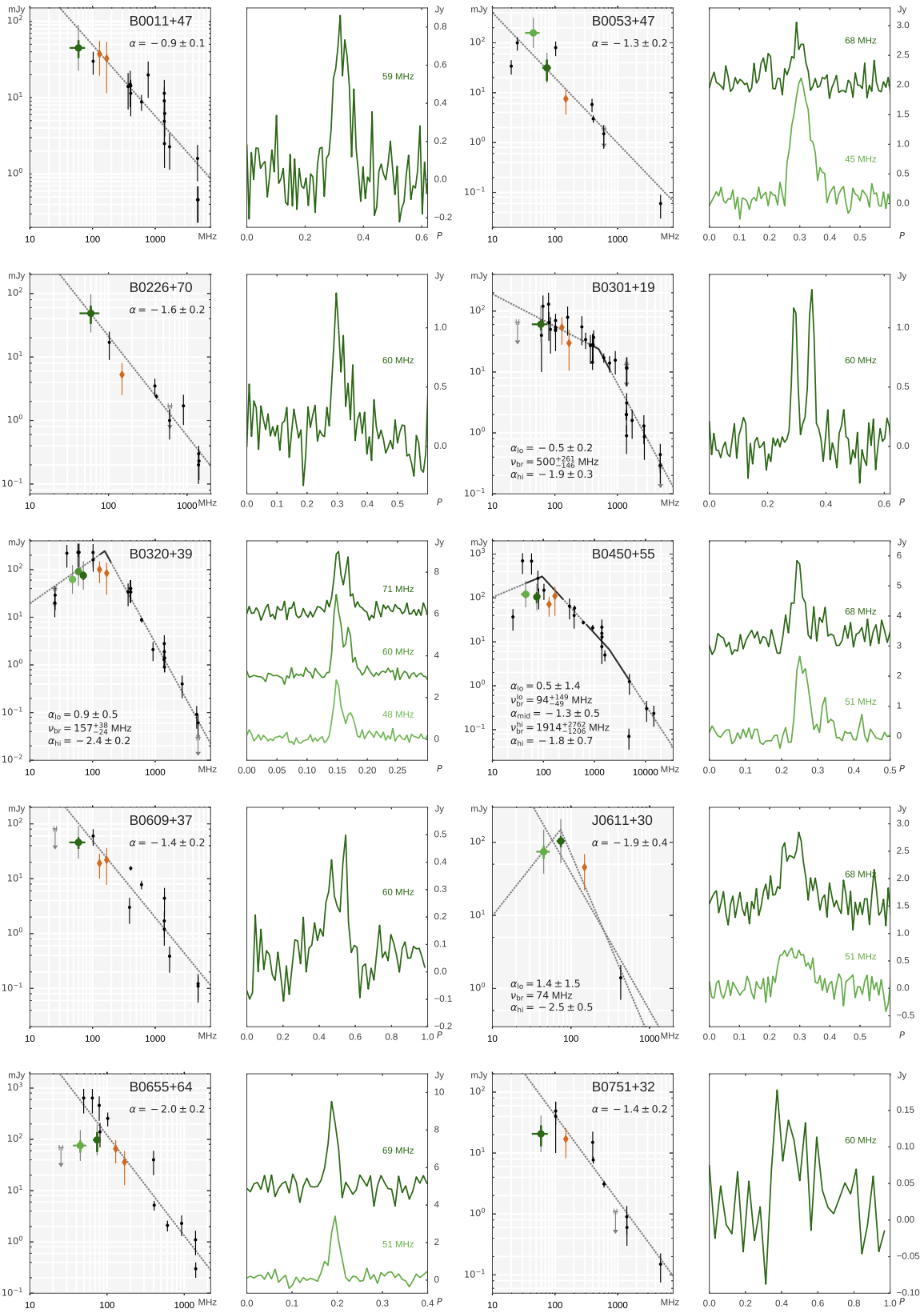

Fig. C.1. For each pair of plots, *Left:* Spectra of radio emission for pulsars detected in the census. Smaller black points with error bars mark literature flux densities, the larger green dots show the LOFAR LBA census measurements at various frequencies (with the horizontal errorbars indicating the frequency span of a given census measurement), brown diamonds show flux densities from HBA census (B16), and the arrows show upper limits. For the LBA census measurements, thin grey errorbars show ±50% flux uncertainty and thicker green ones show uncertainty due to limited S/N. See text for both census and literature flux density errors and upper limit discussion. In the case of a multiple-PL fit, the uncertainty on the break frequency is marked with a broken black line. *Right:* Flux-calibrated average profiles for LOFAR LBA census observations. Multiple profiles per band are shown with a constant flux offset between separate sub-bands. The choice of the number of sub-bands was defined by the peak S/N ratio of the average profile, the presence of profile evolution within the observing band and the number of previously published flux density values.

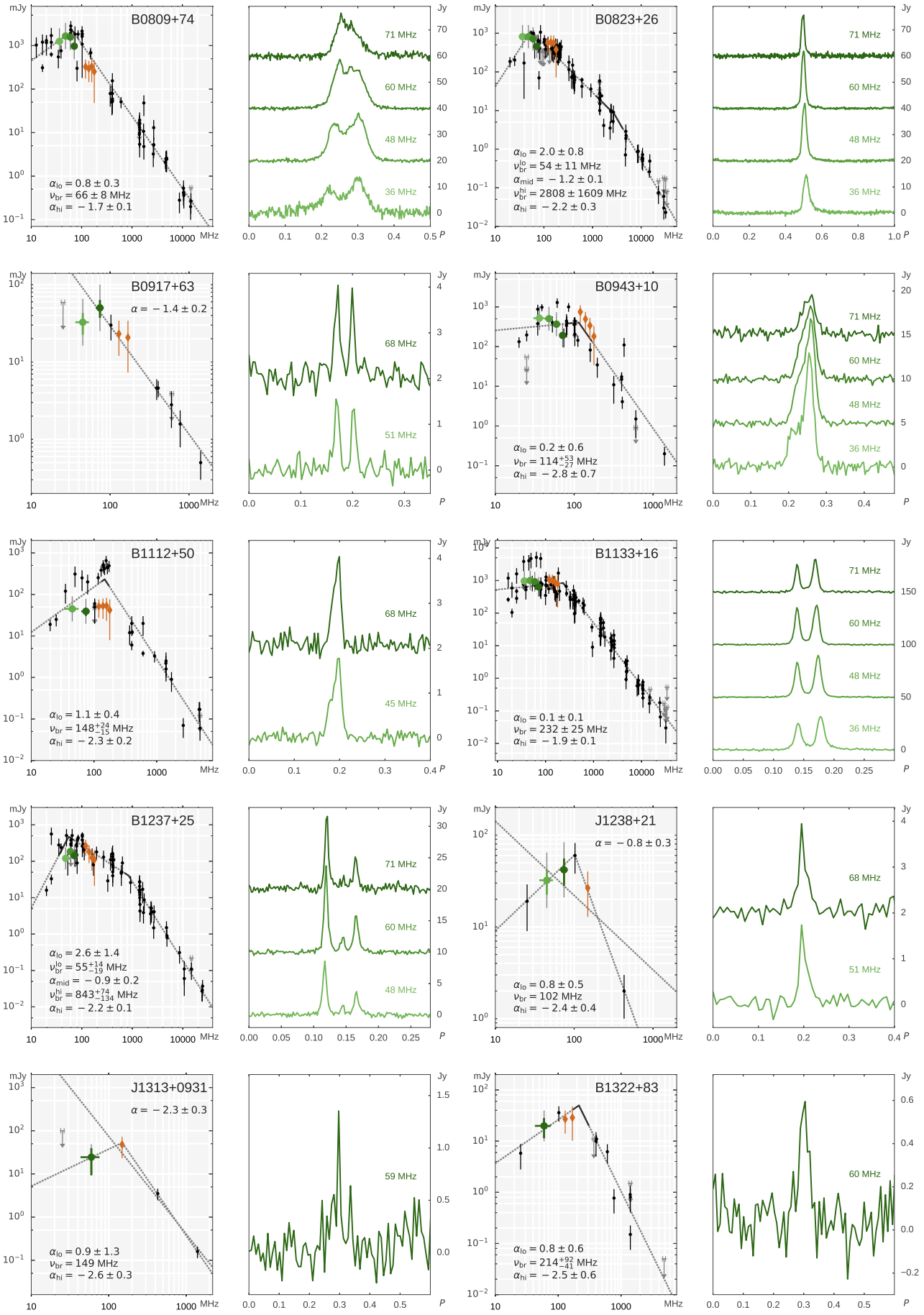

Fig. C.2. See Figure C.1.

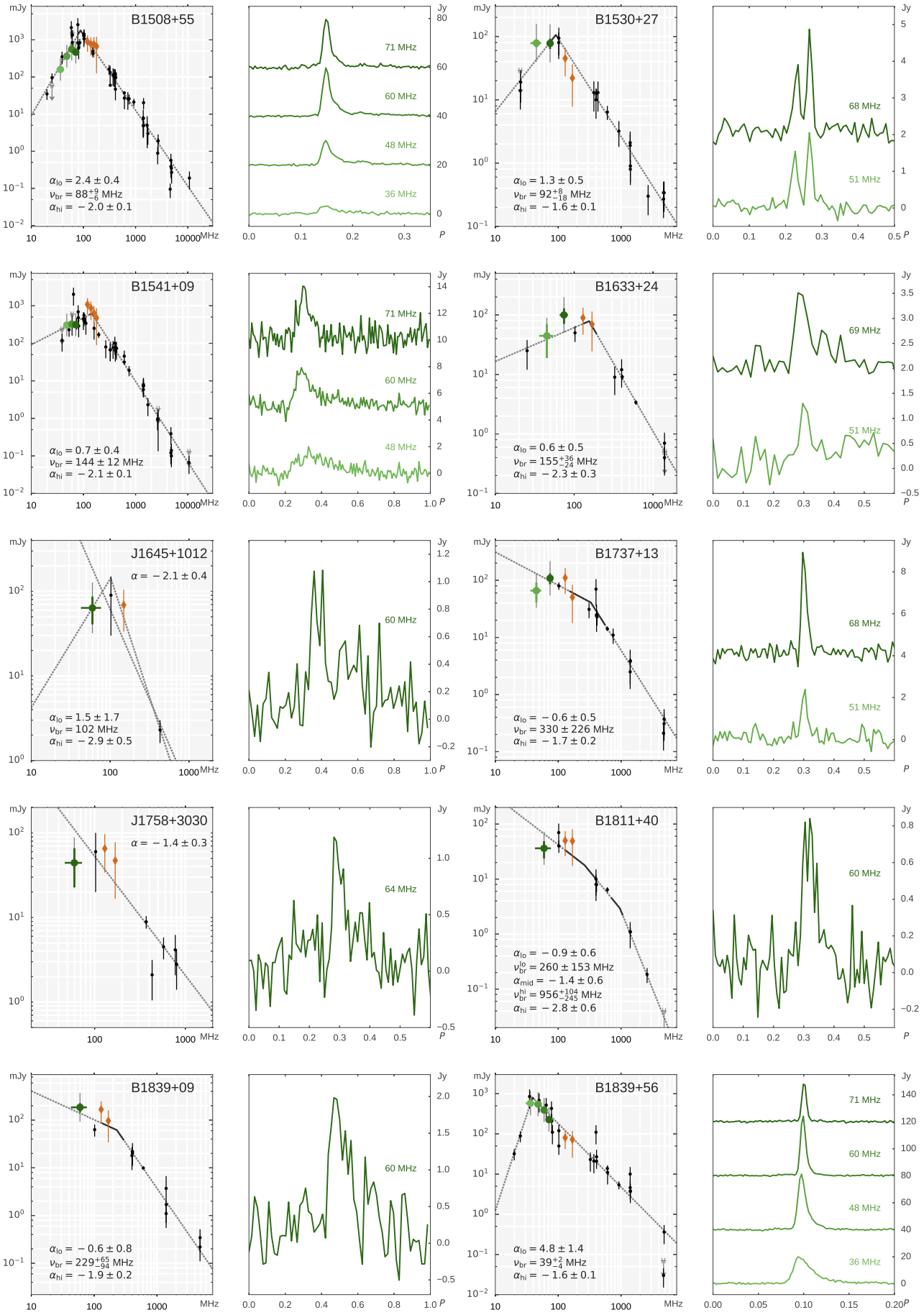

Fig. C.3. See Figure C.1.

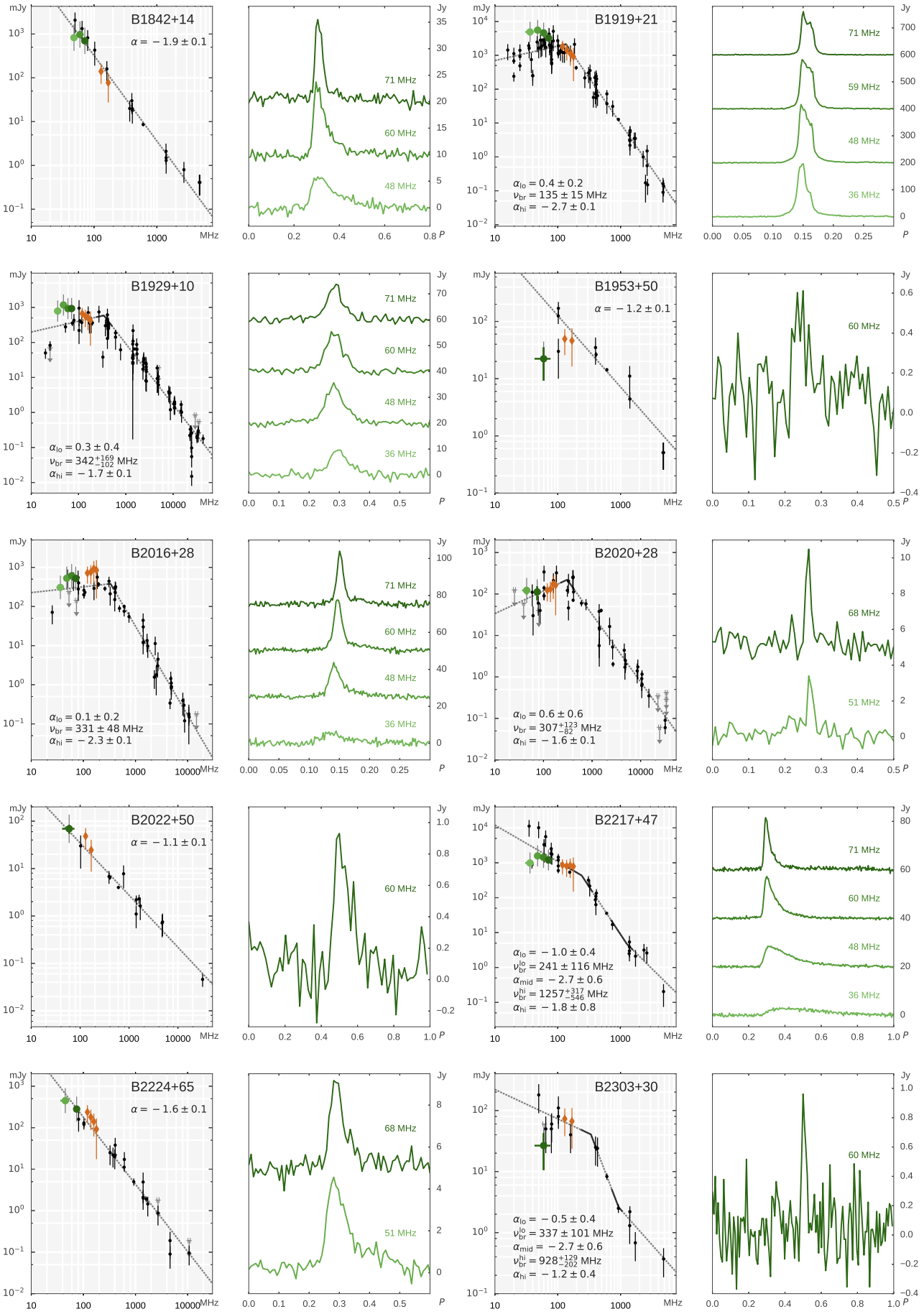

Fig. C.4. See Figure C.1.

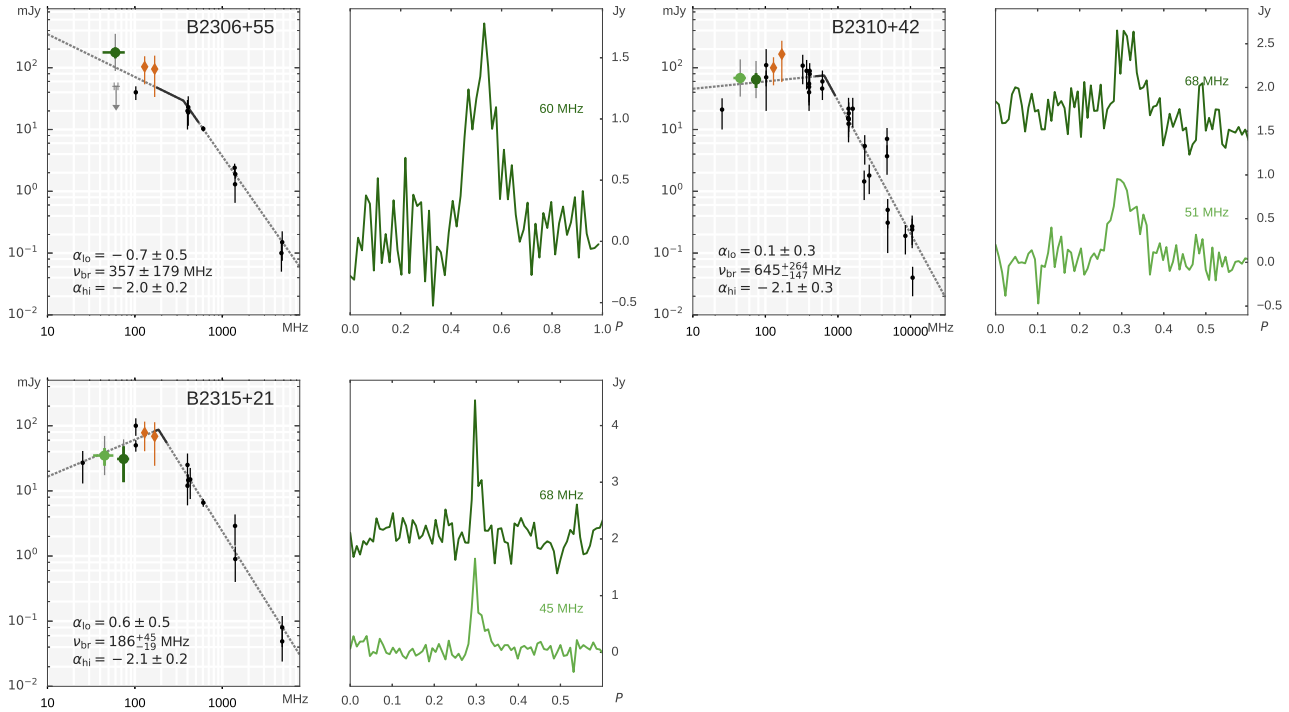

Fig. C.5. See Figure C.1.

References

Barr, E. D., Champion, D. J., Kramer, M., et al. 2013, MNRAS, 435, 2234
Bartel, N., Sieber, W., & Wielebinski, R. 1978, A&A, 68, 361
Beskin, V. S. 2018, Physics Uspekhi, 61, 353
Bhat, N. D. R., Rao, A. P., & Gupta, Y. 1999, ApJS, 121, 483
Bietenholz, M. F., Kassim, N., Frail, D. A., et al. 1997, ApJ, 490, 291
Bilous, A. V., Kondratiev, V. I., Kramer, M., et al. 2016, A&A, 591, A134
Bondonneau, L., Grießmeier, J., Theureau, G., Cognard, I., & the NenuFAR-France collaboration. 2019, in Journées scientifiques 2019 d'URSI-France, 1–8
Boyles, J., Lynch, R. S., Ransom, S. M., et al. 2013, ApJ, 763, 80
Bridle, A. H. 1970, Nature, 225, 1035
Camilo, F. & Nice, D. J. 1995, ApJ, 445, 756
Camilo, F., Nice, D. J., Shrauner, J. A., & Taylor, J. H. 1996, ApJ, 469, 819
Champion, D. J., Lorimer, D. R., McLaughlin, M. A., et al. 2005, MNRAS, 363, 929
Cordes, J. M., Bhat, N. D. R., Hankins, T. H., McLaughlin, M. A., & Kern, J. 2004, ApJ, 612, 375
Damashek, M., Taylor, J. H., & Hulse, R. A. 1978, ApJ, 225, L31
Davies, J. G., Lyne, A. G., & Seiradakis, J. H. 1977, MNRAS, 179, 635
Dembska, M., Kijak, J., Jessner, A., et al. 2014, MNRAS, 445, 3105
Deshpande, A. A. & Radhakrishnan, V. 1992, Journal of Astrophysics and Astronomy, 13, 151
Dewey, R. J., Taylor, J. H., Weisberg, J. M., & Stokes, G. H. 1985, ApJ, 294, L25
Dicke, R. H. 1946, Rev Sci Instrum, 17, 268
Downs, G. S. 1979, ApJS, 40, 365
Downs, G. S., Reichley, P. E., & Morris, G. A. 1973, ApJ, 181, L143
Fomalont, E. B., Goss, W. M., Lyne, A. G., Manchester, R. N., & Justtanont, K. 1992, MNRAS, 258, 497
Gould, D. M. 1994, PhD thesis, , Univ. of Manchester, (1994)
Hamaker, J. P. 2006, A&A, 456, 395
Han, J. L., Demorest, P. B., van Straten, W., & Lyne, A. G. 2009, ApJS, 181, 557
Haslam, C. G. T., Salter, C. J., Stoffel, H., & Wilson, W. E. 1982, A&AS, 47, 1
Hewish, A., Bell, S. J., Pilkington, J. D. H., Scott, P. F., & Collins, R. A. 1968, Nature, 217, 709
Hobbs, G., Faulkner, A., Stairs, I. H., et al. 2004, MNRAS, 352, 1439
Hotan, A. W., van Straten, W., & Manchester, R. N. 2004, Proc. Astron. Soc., 21, 302
Hunter, J. D. 2007, Computing In Science & Engineering, 9, 90
Izvekova, V. A., Kuzmin, A. D., Malofeev, V. M., & Shitov, I. P. 1981, Ap&SS, 78, 45
Izvekova, V. A., Kuz'min, A. D., Malofeev, V. M., & Shitov, Y. P. 1979, Soviet Ast., 23, 179
Jankowski, F., van Straten, W., Keane, E. F., et al. 2018, MNRAS, 473, 4436
Johnston, S., Karastergiou, A., & Willett, K. 2006, MNRAS, 369, 1916
Kaplan, D. L., Condon, J. J., Arzoumanian, Z., & Cordes, J. M. 1998, ApJS, 119, 75
Karuppusamy, R., Stappers, B. W., & Serylak, M. 2011, A&A, 525, A55
Kijak, J., Gupta, Y., & Krzeszowski, K. 2007, A&A, 462, 699
Kijak, J., Kramer, M., Wielebinski, R., & Jessner, A. 1998, A&AS, 127, 153
Kondratiev, V. I., Verbiest, J. P. W., Hessels, J. W. T., et al. 2016, A&A, 585, A128
Kramer, M., Jessner, A., Doroshenko, O., & Wielebinski, R. 1997, ApJ, 488, 364
Kramer, M., Xilouris, K. M., Jessner, A., Wielebinski, R., & Timofeev, M. 1996, A&A, 306, 867
Krzeszowski, K., Maron, O., Słowikowska, A., Dyks, J., & Jessner, A. 2014, MNRAS, 440, 457
Kuzmin, A. D., Malofeev, V. M., Izvekova, V. A., Sieber, W., & Wielebinski, R. 1986, A&A, 161, 183
Kuz'min, A. D., Malofeev, V. M., Shitov, Y. P., et al. 1978, MNRAS, 185, 441
Lane, W. M., Cotton, W. D., van Velzen, S., et al. 2014, MNRAS, 440, 327
Lawson, K. D., Mayer, C. J., Osborne, J. L., & Parkinson, M. L. 1987, MNRAS, 225, 307
Lazarus, P., Karuppusamy, R., Graikou, E., et al. 2016, MNRAS, 458, 868
Lewandowski, W., Wolszczan, A., Feiler, G., Konacki, M., & Sołtysiński, T. 2004, ApJ, 600, 905
Löhmer, O., Jessner, A., Kramer, M., Wielebinski, R., & Maron, O. 2008, A&A, 480, 623
Loi, S. T., Murphy, T., Bell, M. E., et al. 2015, MNRAS, 453, 2731
Lommen, A. N., Zepka, A., Backer, D. C., et al. 2000, ApJ, 545, 1007
Lorimer, D. R. & Kramer, M. 2005, Handbook of Pulsar Astronomy (Cambridge University Press)
Lorimer, D. R., Xilouris, K. M., Fruchter, A. S., et al. 2005, MNRAS, 359, 1524
Lorimer, D. R., Yates, J. A., Lyne, A. G., & Gould, D. M. 1995, MNRAS, 273, 411
Lyubarskii, Y. E. & Petrova, S. A. 1996, Astronomy Letters, 22, 399
Malofeev, V. M. 1993, Astronomy Letters, 19, 138
Malofeev, V. M. 1999, Katalog radiospektrov pulsarov [in russian], Pushchino Radio Astronomy Observatory
Malofeev, V. M. & Malov, I. F. 1980, Soviet Ast., 24, 54
Malofeev, V. M., Malov, O. I., & Shchegoleva, N. V. 2000, Astronomy Reports, 44, 436
Malov, I. F. 1979, Soviet Astronomy, 23, 205
Manchester, R. N. 1971, ApJ, 163, L61
Manchester, R. N., Hobbs, G. B., Teoh, A., & Hobbs, M. 2005, AJ, 129, 1993
Manchester, R. N., Lyne, A. G., Taylor, J. H., et al. 1978, MNRAS, 185, 409
Manchester, R. N. & Taylor, J. H. 1981, AJ, 86, 1953
Maron, O., Kijak, J., Kramer, M., & Wielebinski, R. 2000, A&AS, 147, 195
Moffett, D. A. & Hankins, T. H. 1999, ApJ, 522, 1046
Morris, D., Graham, D. A., Sieber, W., Bartel, N., & Thomasson, P. 1981, A&AS, 46, 421
Murphy, T., Kaplan, D. L., Bell, M. E., et al. 2017, PASA, 34, e020
Navarro, J., Anderson, S. B., & Freire, P. C. 2003, ApJ, 594, 943
Rankin, J. M. & Benson, J. M. 1981, AJ, 86, 418
Rankin, J. M., Comella, J. M., Craft, Jr., H. D., et al. 1970, ApJ, 162, 707
Ray, P. S., Thorsett, S. E., Jenet, F. A., et al. 1996, ApJ, 470, 1103
Sayer, R. W., Nice, D. J., & Taylor, J. H. 1997, ApJ, 474, 426
Seiradakis, J. H., Gil, J. A., Graham, D. A., et al. 1995, A&AS, 111, 205
Shimwell, T. W., Tasse, C., Hardcastle, M. J., et al. 2019, A&A, 622, A1
Shrauner, J. A., Taylor, J. H., & Woan, G. 1998, ApJ, 509, 785
Sieber, W. 1973, A&A, 28, 237
Sieber, W. & Wielebinski, R. 1987, A&A, 177, 342
Slee, O. B., Alurkar, S. K., & Bobra, A. D. 1986, Australian Journal of Physics, 39, 103
Stappers, B. W., Hessels, J. W. T., Alexov, A., et al. 2011, A&A, 530, A80
Stinebring, D. R. & Condon, J. J. 1990, ApJ, 352, 207
Stokes, G. H., Segelstein, D. J., Taylor, J. H., & Dewey, R. J. 1986, ApJ, 311, 694
Stovall, K., Ray, P. S., Blythe, J., et al. 2015, ApJ, 808, 156
Taylor, J. H., Manchester, R. N., & Lyne, A. G. 2000, VizieR Online Data Catalog, 7189
Thorsett, S. E., Deich, W. T. S., Kulkarni, S. R., Navarro, J., & Vasisht, G. 1993, ApJ, 416, 182
van Haarlem, M. P., Wise, M. W., Gunst, A. W., et al. 2013, A&A, 556, A2
van Straten, W., Manchester, R. N., Johnston, S., & Reynolds, J. E. 2010, PASA, 27, 104
van Weeren, R. J., Williams, W. L., Hardcastle, M. J., et al. 2016, ApJS, 223, 2
Vivekanand, M., Mohanty, D. K., & Salter, C. J. 1983, MNRAS, 204, 81P
Wang, N., Manchester, R. N., Johnston, S., et al. 2005, MNRAS, 358, 270
Wielebinski, R., Jessner, A., Kramer, M., & Gil, J. A. 1993, A&A, 272, L13
Wijnholds, S. J. & van Cappellen, W. A. 2011, IEEE Transactions on Antennas and Propagation, 59, 1981
Xue, M., Bhat, N. D. R., Tremblay, S. E., et al. 2017, Publications of the Astronomical Society of Australia, 34, e070
Yao, J. M., Manchester, R. N., & Wang, N. 2017, ApJ, 835, 29
Zakharenko, V. V., Vasylieva, I. Y., Konovalenko, A. A., et al. 2013, MNRAS, 431, 3624
Zarka, P., Girard, J. N., Tagger, M., Denis, L., & the LSS team. 2012, in SF2A-2012: Semaine de l'Astrophysique Francaise, 687–694
Zarka, P., Tagger, M., Denis, L., et al. 2015, in International Conference on Antenna Theory and Technique, 13–18
Zarka, P., Tagger, M., et al. 2014, NenuFAR: instrument description and science case, Tech. rep., https://www.researchgate.net/publication/308806477_NenUFAR_Instrument_description
Zhao, R.-S., Wu, X.-J., Yan, Z., et al. 2017, ApJ, 845, 156